Monthly Notices of the Royal Astronomical Society
MNRAS **450,** 3975–3990 (2015) doi:10.1093/mnras/stv909

Unveiling the nature of the γ-ray emitting active galactic nucleus PKS 0521−36

F. D'Ammando,[1,2]★ M. Orienti,[2] F. Tavecchio,[3] G. Ghisellini,[3] E. Torresi,[4] M. Giroletti,[2] C. M. Raiteri,[5] P. Grandi,[4] M. Aller,[6] H. Aller,[6] M. A. Gurwell,[7] G. Malaguti,[4] E. Pian[8] and G. Tosti[9,10]

[1]*Dip. Di Fisica e Astronomia, Università degli Studi di Bologna, Via Ranzani 1, I-40127 Bologna, Italy*
[2]*INAF – Istituto di Radioastronomia, Via Gobetti 101, I-40129 Bologna, Italy*
[3]*INAF – Osservatorio Astronomico di Brera, Via E. Bianchi 46, I-23807 Merate, Italy*
[4]*INAF – Istituto di Astrofisica Spaziale e Fisica Cosmica, Via Gobetti 101, I-40129 Bologna, Italy*
[5]*INAF – Osservatorio Astrofisico di Torino, Via Osservatorio 20, I-10025 Pino Torinese (TO), Italy*
[6]*University of Michigan, Ann Arbor, MI 48109, USA*
[7]*Harvard-Smithsonian Center for Astrophysics, Cambridge, MA 02138, USA*
[8]*Scuola Normale Superiore Pisa, Piazza dei Cavalieri 7, I-56126 Pisa, Italy*
[9]*Dip. di Fisica, Università degli Studi di Perugia, Via A. Pascoli, I-06123 Perugia, Italy*
[10]*INFN – Sezione di Perugia, Via A. Pascoli, I-06123 Perugia, Italy*

Accepted 2015 April 21. Received 2015 April 17; in original form 2015 March 13

ABSTRACT

PKS 0521−36 is an active galactic nucleus (AGN) with uncertain classification. We investigate the properties of this source from radio to γ-rays. The broad emission lines in the optical and ultraviolet bands and steep radio spectrum indicate a possible classification as an intermediate object between broad-line radio galaxies (BLRG) and steep spectrum radio quasars (SSRQ). On pc-scales PKS 0521−36 shows a knotty structure similar to misaligned AGN. The core dominance and the γ-ray properties are similar to those estimated for other SSRQ and BLRG detected in γ-rays, suggesting an intermediate viewing angle with respect to the observer. In this context the flaring activity detected from this source by *Fermi*-Large Area Telescope between 2010 June and 2012 February is very intriguing. We discuss the γ-ray emission of this source in the framework of the structured jet scenario, comparing the spectral energy distribution (SED) of the flaring state in 2010 June with that of a low state. We present three alternative models corresponding to three different choices of the viewing angles $\theta_v = 6^\circ$, 15°, and 20°. We obtain a good fit for the first two cases, but the SED obtained with $\theta_v = 15^\circ$ if observed at a small angle does not resemble that of a typical blazar since the synchrotron emission should dominate by a large factor ($\sim$100) the inverse Compton component. This suggests that a viewing angle between 6° and 15° is preferred, with the rapid variability observed during γ-ray flares favouring a smaller angle. However, we cannot rule out that PKS 0521−36 is the misaligned counterpart of a synchrotron-dominated blazar.

Key words: galaxies: active – galaxies: individual: PKS 0521−36 – galaxies: nuclei – quasars: general – gamma-rays: galaxies – gamma-rays: general.

1 INTRODUCTION

Active galactic nuclei (AGN) are compact regions at the centre of a few per cent of galaxies with a non-stellar emission overwhelming the thermal contribution of the entire galaxy. AGN include a supermassive black hole (SMBH) as central engine, whose strong gravitational potential pulls the surrounding materials inwards, forming a disc of hot plasma. In addition, gas clouds move in the potential well of the SMBH, producing optical and ultraviolet (UV) emission lines. The central region is surrounded by absorbing material in a flattened configuration, idealized as a toroidal shape, located at ∼1–10 pc. In radio-loud objects there is the additional presence of relativistic jets, roughly perpendicular to the disc. According to the Unified Model (Urry & Padovani 1995), AGN types are classified on the basis of the orientation of their jet with respect to the

★ E-mail: dammando@ira.inaf.it

observer. Blazars, usually divided into flat spectrum radio quasars (FSRQ) and BL Lac objects, represent the fraction of AGN with their jet oriented at very small viewing angle, which causes relativistic aberration and emission amplification (Blandford & Rees 1978). Radio galaxies should be the misaligned parent population of blazars. On the basis of their radio morphology and power, radio galaxies are classified as Fanaroff–Riley type I (FR I) or Fanaroff–Riley type II (FR II). Decelerating jets and kpc scale edge-darkened lobes are found in the weaker FR I radio galaxies, while relativistic jets and edge-brightened radio lobes are found in the stronger FR II radio galaxies (Fanaroff & Riley 1974). According to the unification scenario for radio-loud AGN, FR I radio galaxies correspond to BL Lac objects, and FR II radio galaxies are the parent population of FSRQ.

PKS 0521−36 was first classified as an N galaxy (Bolton, Clarke & Ekers 1965), and then a BL Lac object (Danziger et al. 1979; Burbidge & Hewitt 1987). However, this source shows broad and variable nuclear emission lines in optical and UV bands (Ulrich 1981; Scarpa, Falomo & Pian 1995) with equivalent width (EW) much larger than 5 Å (rest frame), the threshold historically proposed to distinguish between BL Lac objects and FSRQ (e.g. Stickel et al. 1991; Stocke et al. 1991). This suggests that PKS 0521−36 is a misclassified AGN. For this source, a large-scale optical jet well aligned with the kiloparsec radio jet was observed, with a clear correspondence between the radio and optical structures (Scarpa et al. 1999, and references therein). In radio and optical bands the jet resembles that of the nearby radio galaxy M87 (e.g. Sparks, Biretta & Macchetto 1994). *Chandra* detected the X-ray counterpart of the innermost 2-arcsec jet (Birkinshaw, Worrall & Hardcastle 2002).

In the γ-ray energy range PKS 0521−36 was tentatively detected by the Energetic Gamma-Ray Experiment Telescope (EGRET) on board the *Compton Gamma-Ray Observatory* in Phase 1 (Lin, Bertsch & Dingus 1995), but it was not included in the Third EGRET catalogue (Hartman et al. 1999). No beaming effect is needed for the core brightness temperature estimated in radio, consistent with the non-detection of superluminal motion (Tingay & Edwards 2002). By modelling the spectral energy distribution (SED) and taking into account its radio characteristics, Pian et al. (1996) derived a viewing angle of 30° with a bulk Lorentz factor of 1.2. Very Long Baseline Array (VLBA) image showed that the same position angle (PA) found on the parsec-scale jet is maintained, without any significant bending, over three orders of magnitude of length scale (Giroletti et al. 2004). This may be a further indication of a relatively large viewing angle. For a plausible Lorentz factor of $\Gamma = 5$, Giroletti et al. (2004) derive a viewing angle θ in the range 21°–27°.

On 2010 June 17, a strong γ-ray flare from PKS 0521−36 was detected by the Large Area Telescope (LAT) on board the *Fermi Gamma-ray Space Telescope* satellite (Iafrate, Longo & D'Ammando 2010), triggering a *Swift* follow-up observation that confirmed the high activity of the source in optical, UV, and X-rays (D'Ammando et al. 2010). In this paper we investigate the nature of this object and its emission mechanisms by the analysis of multifrequency data collected from radio to γ-rays, focusing in particular on the 2010 June flaring activity.

The paper is organized as follows. In Section 2, we report the LAT data analysis and results. In Section 3, we report the results of the new *Swift* and archival *XMM–Newton* and *Chandra* data analysis. Radio data collected by the VLBA, Very Large Array (VLA), University of Michigan Radio Astronomy Observatory (UMRAO), and Submillimeter Array (SMA) are presented in Section 4. In Section 5, we discuss the source properties from radio to γ-rays. In Section 6, we discuss the modelling of the overall SED and draw our conclusions in Section 7.

Throughout the paper the quoted uncertainties are given at the 1σ level, unless otherwise stated. The photon indices are parametrized as $\mathrm{d}N/\mathrm{d}E \propto E^{-\Gamma_\nu}$, where Γ_ν is the photon index at the different energy bands. We used a Λ cold dark matter cosmology with $H_0 = 71\,\mathrm{km\,s^{-1}\,Mpc^{-1}}$, $\Omega_\Lambda = 0.73$, and $\Omega_\mathrm{m} = 0.27$ (Komatsu et al. 2009). The corresponding luminosity distance at $z = 0.056$ is $d_L = 246.8$ Mpc and 1 arcsec corresponds to a projected size of 1.073 kpc.

2 *Fermi*-LAT DATA

The LAT on board the *Fermi* satellite is a γ-ray telescope operating from 20 MeV to >300 GeV, with a large peak effective area (∼8000 cm^2 for 1 GeV photons), an energy resolution typically ∼10 per cent, and a field of view of about 2.4 sr with single-photon angular resolution (68 per cent containment radius) of 0°.6 at $E = 1$ GeV on-axis. Details about the LAT are given by Atwood et al. (2009).

The LAT data reported in this paper were collected over the first 4 yr of *Fermi* operation, from 2008 August 4 (MJD 54682) to 2012 August 4 (MJD 56143) in the 0.1–100 GeV energy range. During this time, the *Fermi* observatory operated almost entirely in survey mode. The analysis was performed with the SCIENCETOOLS software package version v9r32p5.[1] Only events belonging to the 'Source' class were used. The time intervals when the rocking angle of the LAT was greater than 52° were rejected. In addition, a cut on the zenith angle (<100°) was applied to reduce contamination from the Earth limb γ-rays, which are produced by cosmic rays interacting with the upper atmosphere. The spectral analysis was performed with the instrument response functions P7REP_SOURCE_V15 using an unbinned maximum likelihood method implemented in the tool GTLIKE. Isotropic ('ISO_SOURCE_V05.TXT') and Galactic diffuse emission ('GLL_IEM_V05_REV1.FIT') components were used to model the background.[2] The normalizations of both components were allowed to vary freely during the spectral fitting.

We analysed a region of interest of 10° radius centred at the location of PKS 0521−36. We evaluated the significance of the γ-ray signal from the source by means of the maximum likelihood test statistic TS = $2(\log L_1 - \log L_0)$, where L is the likelihood of the data given the model with (L_1) or without (L_0) a point source at the position of PKS 0521−36 (e.g. Mattox et al. 1996). The source model used in GTLIKE includes all of the point sources from the third *Fermi*-LAT catalogue (3FGL; Acero et al. 2015) that fall within 15° of the source. The spectra of these sources were parametrized by power law (PL), log parabola (LP), or exponentially cut-off PL model, as in the 3FGL catalogue. A first maximum likelihood analysis was performed to remove from the model faint sources with fluxes lower than 1×10^{-8} photons cm^{-2} s^{-1} for avoiding possible problems of fit convergence. A second maximum likelihood analysis was performed on the updated source model. In the fitting procedure, the normalization factors and the spectral parameters of the sources lying within 10° of PKS 0521−36 were left as free parameters. For the sources located between 10° and 15° from our target, we kept the normalization and the spectral parameters fixed to the values from the 3FGL catalogue.

[1] http://fermi.gsfc.nasa.gov/ssc/data/analysis/
[2] http://fermi.gsfc.nasa.gov/ssc/data/access/lat/BackgroundModels.html

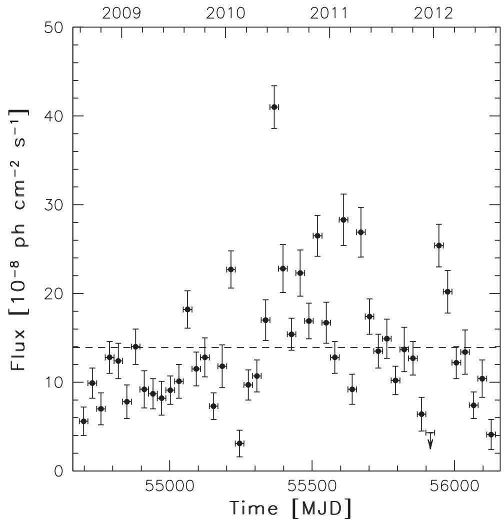

Figure 1. LAT light curve of PKS 0521−36 for $E > 100$ MeV using a PL model with photon index fixed to $\Gamma_\gamma = 2.45$ in monthly time bins from 2008 August 4 to 2012 August 4 (MJD 54682–56143). The downward arrow represents a 2σ upper limit. The dashed line indicates the average flux over the whole period.

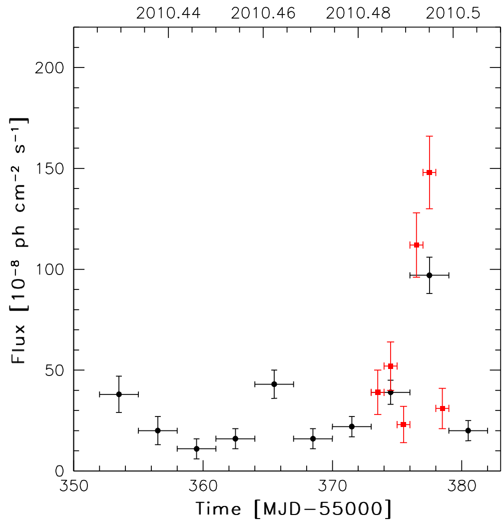

Figure 2. LAT light curve of PKS 0521−36 for $E > 100$ MeV using a PL model with photon index fixed to $\Gamma_\gamma = 2.16$ in 3-d (black circles) and 1-d (red squares) time bins from 2010 June 4 to July 4 (MJD 55351–55381).

The fit with a PL model, $\mathrm{d}N/\mathrm{d}E \propto (E/E_0)^{-\Gamma_\gamma}$, to the data integrated over 48 months of *Fermi* operation (2008 August–2012 August) in the 0.1–100 GeV energy range results in TS = 4945, with an integrated average flux of $(13.9 \pm 0.4) \times 10^{-8}$ photons cm^{-2} s^{-1}, and a photon index $\Gamma_\gamma = 2.45 \pm 0.02$. Fig. 1 shows the γ-ray light curve of the first 4 yr of *Fermi* observations of PKS 0521−36 built using 1-month time bins. For each time bin, the photon index was frozen to the value resulting from the likelihood analysis over the whole period. The systematic uncertainty in the flux is dominated by the systematic uncertainty in the effective area (Ackermann et al. 2012), which amounts to 10 per cent below 100 MeV, decreasing linearly with the logarithm of energy to 5 per cent between 316 MeV and 10 GeV, and increasing linearly with the logarithm of energy up to 15 per cent at 1 TeV.[3]

PKS 0521−36 has been quite active since 2009 September. An increase of the γ-ray flux was observed in 2010 January, and subsequently a significant flaring activity occurred in 2010 June. A second light curve focusing on the period of the highest activity (2010 June 4–July 4; MJD 55351–55381) was built with 3- and 1-d time bins (Fig. 2). Leaving the photon index free to vary during 2010 June 4–July 4, the global fit results in TS = 901 and a photon index $\Gamma_\gamma = 2.16 \pm 0.05$, indicating a harder-when-brighter behaviour, similar to what was observed in FSRQ and low-synchrotron-peaked BL Lacs (Abdo et al. 2010b). The peak of the emission was observed on 2010 June 30 (MJD 55377), with a flux of $(148 \pm 18) \times 10^{-8}$ photons cm^{-2} s^{-1} in the 0.1–100 GeV energy range, a factor of ~11 higher than the average γ-ray flux during 2008 August–2012 August. The corresponding apparent isotropic γ-ray peak luminosity is 8.5×10^{45} erg s^{-1}. During the period 2010 June 4–July 4, the fit with an LP model, $\mathrm{d}N/\mathrm{d}E \propto (E/E_0)^{-\alpha-\beta\,\log(E/E_0)}$, in the 0.1–100 GeV energy range results in TS = 902, with a spectral slope $\alpha = 2.14 \pm 0.07$ at the decorrelation energy $E_0 = 384$ MeV, and a curvature parameter $\beta = 0.02 \pm 0.02$ (Table 1). We used a likelihood ratio test (LRT) to check a PL model (null hypothesis) against an LP model (alternative hypothesis). Following Nolan et al. (2012), these values may be compared by defining the curvature test statistic $\mathrm{TS_{curve}} = (\mathrm{TS_{LP}} - \mathrm{TS_{PL}})$. The LRT results in $\mathrm{TS_{curve}} = 1$, corresponding to a $\sim 1\sigma$ difference, indicating no significant curvature in the γ-ray spectrum during the flaring period. Considering the entire period 2008 August 4–2012 August 4 the fit with an LP results in TS = 4962, with a spectral slope $\alpha = 2.40 \pm 0.05$ at the decorrelation energy $E_0 = 384$ MeV, a curvature parameter $\beta = 0.07 \pm 0.02$, and an average flux of $(13.2 \pm 0.8) \times 10^{-8}$ photons cm^{-2} s^{-1} (Table 1), consistent with the results reported in the 3FGL (Acero et al. 2015). The LRT results in $\mathrm{TS_{curve}} = 17$, corresponding to a $\sim 4\sigma$ difference (for 1 degree of freedom). This indicates a significant curvature in the γ-ray spectrum over the entire period, contrary to what is observed in shorter periods.

In addition to the 3- and 1-d light curves shown in Fig. 2, we also computed a light curve in 12-h bins during the period of brightest flux (2010 June 26–July 1). In this light curve (not shown) we note a significant increase from $(49 \pm 15) \times 10^{-8}$ to $(193 \pm 29) \times 10^{-8}$ photons cm^{-2} s^{-1} between the first and second 12-h bin on 2010 June 29. The peak flux at 12-h time-scale corresponds to an apparent isotropic γ-ray luminosity of 1.1×10^{46} erg s^{-1}.

We investigated whether spectral changes are present during the period 2008 August–2012 August, using a PL model. We plot the photon index against the γ-ray flux above 100 MeV estimated on a monthly time-scale. Unlikely as in Fig. 1, in which the photon indices are fixed, for each time bin the spectral parameters for PKS 0521−36 and for all the sources within 10° from it were left free to vary. No obvious relation between flux and photon index was observed (Fig. 3).

Other high-activity periods of PKS 0521−36 have been observed in 2011 February and April, and 2012 January. In particular, in 2011 April the source was not detected for the first part of the month, and then a rapid increase of flux from $(25 \pm 13) \times 10^{-8}$ to $(185 \pm 29) \times 10^{-8}$ photons cm^{-2} s^{-1} was observed between 2011 April 23 and 24 (Fig. 4) with $\Gamma_\gamma = 2.33$, the value obtained leaving the photon index free to vary on monthly time-scales (see Fig. 3, bottom panel). As for Fig. 2, we investigated the 12-h light curve during the period of brightest flux (2011 April 22–26). We note that

[3] http://fermi.gsfc.nasa.gov/ssc/data/analysis/LAT_caveats.html

Table 1. Unbinned likelihood spectral fit results.

Time period (MJD)	Time period (UT)	PL Γ	PL TS_{PL}	LP α	LP β	LP TS_{LP}
54682–56143	2008-08-04/2012-08-04	2.45 ± 0.02	4945	2.40 ± 0.05	0.07 ± 0.02	4962
55351–55381	2010-06-04/2010-07-04	2.16 ± 0.05	901	2.14 ± 0.07	0.02 ± 0.02	902

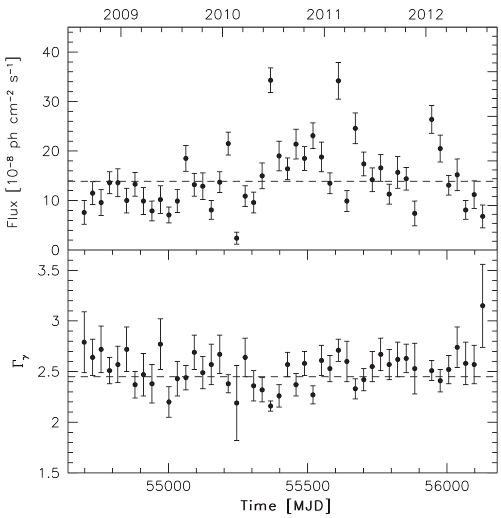

Figure 3. The 0.1–100 GeV flux in units of 10^{-8} photons cm^{-2} s^{-1} (top panel) and the photon index from a PL model (bottom panel) for PKS 0521−36 using 1-month time bins. The dashed line in both panels represents the mean value.

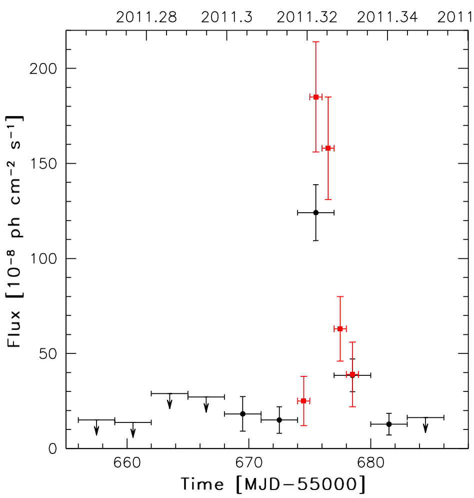

Figure 4. LAT light curve of PKS 0521−36 for $E > 100$ MeV using a PL model with photon index fixed to $\Gamma_\gamma = 2.33$ in 3-d (black circles) and 1-d (red squares) time bins from 2011 April 6 to May 5 (MJD 55657–55686). The downward arrow represents a 2σ upper limit.

an increase from $(129 \pm 32) \times 10^{-8}$ to $(275 \pm 56) \times 10^{-8}$ photons cm^{-2} s^{-1} was observed between the first and second 12-h bin on 2011 April 24. The peak flux at 12-h time-scale corresponds to an apparent isotropic γ-ray luminosity of 1.2×10^{46} erg s^{-1}. It is interesting to note that during the 2010 June and 2011 April flares the peaks show a moderately asymmetric profile (i.e. different rising and decaying times) on a daily time-scale. In particular, the rapid increase observed in 2011 April suggests a cooling time longer than the light crossing time R/c related to fast injection of accelerated particles and a slower radiative cooling.

Analysing the LAT events with $E > 10$ GeV collected over 2008 August–2012 August the fit results in TS = 89, a photon index $\Gamma_\gamma = 2.71 \pm 0.27$, and a flux of $(1.43 \pm 0.36) \times 10^{-10}$ photons cm^{-2} s^{-1}. By means of the GTSRCPROB tool, we estimated that the highest energy photon emitted from PKS 0521−36 (with probability >90 per cent of being associated with the source) was observed on 2010 August 17 (MJD 55425), at a distance of 0.°03 from the source and with an energy of 73 GeV.

3 X-RAY, UV, AND OPTICAL DATA

3.1 *Swift* observations

The *Swift* satellite (Gehrels et al. 2004) performed 19 observations of PKS 0521−36 between 2005 May 26 and 2011 September 5. In particular five observations were triggered by the γ-ray activity observed in 2010 June. The observations were performed with all three on-board instruments: the X-ray Telescope (XRT; Burrows et al. 2005, 0.2–10.0 keV), the UV/Optical Telescope (UVOT; Roming et al. 2005, 170–600 nm), and the Burst Alert Telescope (BAT; Barthelmy et al. 2005, 15–150 keV).

3.1.1 *Swift-BAT*

The hard X-ray flux of this source is below the sensitivity of the BAT instrument for the short exposure time of the individual *Swift* observations. However, PKS 0521−36 is detected in the BAT 70-month catalogue,[4] generated from the all-sky survey in the time period 2004 November–2010 August. The data reduction and extraction procedure of the eight-channel spectrum is described in Baumgartner et al. (2013). The 14–195 keV spectrum is described by a PL with photon index of 1.83 ± 0.15 ($\chi^2_{\rm red} = 2.87$, 5 d.o.f.). The resulting 14–195 keV flux is $(3.5 \pm 0.3) \times 10^{-11}$ erg cm^{-2} s^{-1}.

3.1.2 *Swift-XRT*

The XRT data were processed with standard procedures (XRTPIPELINE v0.12.6), filtering, and screening criteria by using the HEASOFT package (v6.13). The data were collected in photon counting mode in all the observations, and only XRT event grades 0–12 were selected. Source events were extracted from a circular region with a radius of 20 pixels (1 pixel = 2.36 arcsec), while background events were extracted from a circular region with radius of 50 pixels away from the source region. Some observations showed a source count rate >0.5 counts s^{-1}; thus pile-up correction was required. For those observations we extracted the source events from an annular region with an inner radius of 3 pixels [estimated by means of the point spread function (PSF) fitting technique] and an outer radius of 30 pixels, while background events were extracted from an annular

[4] http://heasarc.gsfc.nasa.gov/results/bs70mon

Table 2. Log and fitting results of *Swift*-XRT observations of PKS 0521−36. A PL model with N_H fixed to the Galactic column density was used.

Date (MJD)	Date (UT)	Net exposure time (s)	Γ_X	Flux (2–10 keV) (10^{-11} erg cm^{-2} s^{-1})	χ^2_{red} (d.o.f.)
53516	2005-26-05	900	1.72 ± 0.14	1.34 ± 0.12	1.034 (17)
54498	2008-02-02	4832	1.61 ± 0.06	1.32 ± 0.06	1.062 (88)
54503/04	2008-02-07/08	4947	1.59 ± 0.06	1.18 ± 0.06	0.918 (64)
54509	2008-02-13	2901	1.55 ± 0.09	1.27 ± 0.08	0.869 (41)
55260	2010-03-05	1681	1.67 ± 0.12	0.88 ± 0.11	1.082 (20)
55263	2010-03-08	2405	1.62 ± 0.10	1.20 ± 0.10	0.887 (35)
55366	2010-06-19	2759	1.62 ± 0.08	1.86 ± 0.10	1.018 (42)
55370	2010-06-23	3951	1.57 ± 0.07	2.38 ± 0.14	1.020 (57)
55382	2010-07-05	2774	1.64 ± 0.09	1.97 ± 0.13	1.089 (42)
55386	2010-07-09	2904	1.66 ± 0.09	2.06 ± 0.15	1.073 (37)
55390	2010-07-13	2822	1.60 ± 0.08	1.90 ± 0.11	0.992 (40)
55626	2011-03-06	1126	1.78 ± 0.16	1.30 ± 0.18	0.776 (13)
55627	2011-03-07	2015	1.75 ± 0.10	1.49 ± 0.09	0.899 (32)
55661/02	2011-04-09/10	1868	1.62 ± 0.08	1.34 ± 0.09	0.968 (34)
55804/05	2011-08-31/09-01	1628	1.79 ± 0.12	0.80 ± 0.08	1.117 (17)
55809	2011-09-05	1393	1.67 ± 0.12	1.77 ± 0.15	0.928 (21)

region centred on the source with radii of 70 and 120 pixels. Ancillary response files were generated with XRTMKARF, and account for different extraction regions, vignetting, and PSF corrections. We used the spectral redistribution matrices in the calibration data base maintained by High Energy Astrophysics Science Archive Research Center (HEASARC).[5] The data collected during 2008 February 7 and 8, 2011 April 9 and 10, and 2011 August 31 and September 1 were summed in order to have enough statistics to obtain a good spectral fit.

We fit the spectra in the 0.3–10 keV energy range with an absorbed PL using the photoelectric absorption model TBABS (Wilms, Allen & McCray 2000), with a neutral hydrogen column density fixed to its Galactic value (3.58×10^{20} cm^{-2}; Kalberla et al. 2005). Considering the lower statistics with respect to the *XMM–Newton* and *Chandra* observations, more detailed spectral modelling was not performed with the XRT observations. The fit results are reported in Table 2. *Swift*-XRT observed the source during 2005–2011 with a 2–10 keV flux in the range (0.8–2.4) $\times 10^{-11}$ erg cm^{-2} s^{-1}. No significant change of the photon index was observed. During 2010 mid-June, in the period of highest γ-ray activity, an increase of the X-ray flux was observed, but not accompanied by significant hardening of the spectrum. Furthermore, by comparing the 2–10 keV flux observed by *Swift*-XRT with those observed by *Chandra* (see Section 3.2 for details) we noted a significant increase of the flux (a factor of ∼10) between 1999 and 2011 (Fig. 5).

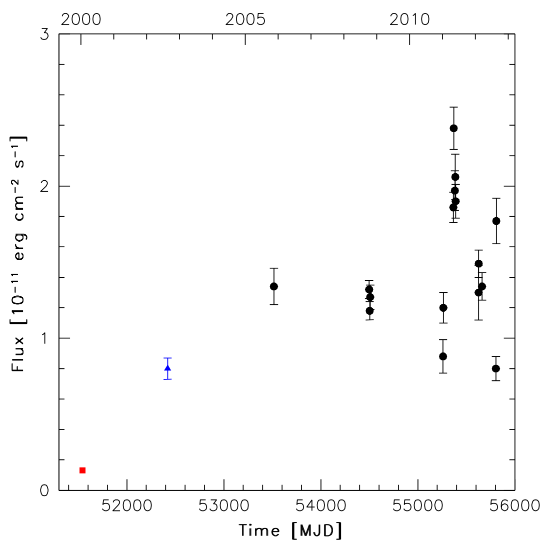

Figure 5. X-ray light curve in the 2–10 keV energy range during the period 1999–2012. Square: *Chandra*; triangle: *XMM–Newton*; circles: *Swift*-XRT.

3.1.3 *Swift-UVOT*

UVOT observed PKS 0521−36 in all its optical (v, b, and u) and UV ($uvw1$, $uvm2$, and $uvw2$) photometric filters. Data were reduced with the HEASOFT package v6.14 and the 20130118 CALDB-UVOTA release. We extracted the source counts from a circle with 5 arcsec radius centred on the source. Background counts were derived from an annular region centred on the source with 15 and 20 arcsec radii. The observed magnitudes are reported in Table 3. During 2008–2011 the difference between the maximum and minimum magnitude is 0.7, 0.9, 0.7, 1.3, 1.3, and 1.4 mag from the v to the $uvw2$ band, with the peak of the activity observed on 2010 June 19.

As in e.g. Raiteri et al. (2011), we calculated the effective wavelengths, count-to-flux conversion factors (CF_Λ), and amount of Galactic extinction in the UVOT bands (A_Λ) by convolving the physical quantities with a PL fit to the source flux and with the UVOT effective areas. In particular, to derive the A_Λ we adopted the mean extinction law by Cardelli, Clayton & Mathis (1989) with $R_V = A_V/E(B-V) = 3.1$ (the standard value for the diffuse interstellar medium), as well as $A_V = 0.112$ from Schlafly & Finkbeiner (2011). To obtain the UVOT dereddened fluxes we multiplied the count rates by the CF_Λ and corrected for the corresponding Galactic extinction values A_Λ.

3.2 *XMM–Newton* and *Chandra* observations

PKS 0521–36 was observed by the *Chandra* and *XMM–Newton* X–ray satellites on 1999 December 31 (MJD 51543) and 2002

[5] http://heasarc.gsfc.nasa.gov/

Table 3. Results of *Swift*-UVOT observations of PKS 0521−36 in observed magnitude.

Date (MJD)	Date (UT)	v (mag)	b (mag)	u (mag)	$w1$ (mag)	$m2$ (mag)	$w2$ (mag)
53516	2005-05-26	–	–	–	15.94 ± 0.02	–	–
54498	2008-02-02	–	–	–	15.11 ± 0.02	–	–
54503	2008-02-07	–	–	–	15.67 ± 0.04	–	–
54504	2008-02-08	15.16 ± 0.03	15.89 ± 0.03	15.41 ± 0.03	15.58 ± 0.03	15.71 ± 0.03	15.82 ± 0.03
54509	2008-02-13	15.15 ± 0.03	15.93 ± 0.03	15.42 ± 0.03	15.59 ± 0.03	15.69 ± 0.04	15.83 ± 0.03
55260	2010-03-05	14.94 ± 0.04	15.68 ± 0.03	15.13 ± 0.03	15.34 ± 0.03	15.44 ± 0.04	15.59 ± 0.03
55263	2010-03-08	–	–	–	15.18 ± 0.02	–	–
55366	2010-06-19	14.58 ± 0.03	15.12 ± 0.02	14.49 ± 0.03	14.54 ± 0.02	14.63 ± 0.03	14.54 ± 0.03
55370	2010-06-23	14.98 ± 0.03	15.67 ± 0.03	15.18 ± 0.03	15.36 ± 0.03	15.51 ± 0.03	15.63 ± 0.03
55382	2010-07-05	14.83 ± 0.03	15.48 ± 0.03	14.93 ± 0.03	15.11 ± 0.03	15.17 ± 0.03	15.27 ± 0.03
55386	2010-07-09	14.93 ± 0.03	15.61 ± 0.03	15.08 ± 0.03	15.28 ± 0.03	15.33 ± 0.03	15.46 ± 0.03
55390	2010-07-13	15.09 ± 0.03	15.87 ± 0.03	15.33 ± 0.03	15.44 ± 0.03	15.67 ± 0.04	15.74 ± 0.03
55626	2011-03-06	15.27 ± 0.05	16.05 ± 0.04	15.58 ± 0.04	15.71 ± 0.04	15.90 ± 0.05	15.97 ± 0.04
55627	2011-03-07	–	–	–	15.74 ± 0.02	–	–
55661	2011-04-09	15.14 ± 0.05	15.95 ± 0.04	15.50 ± 0.05	15.59 ± 0.05	15.76 ± 0.06	15.83 ± 0.04
55662	2011-04-10	15.10 ± 0.05	15.90 ± 0.04	15.39 ± 0.04	15.56 ± 0.05	15.69 ± 0.05	15.83 ± 0.04
55804	2011-08-31	–	–	15.63 ± 0.03	–	–	–
55805	2011-09-01	15.23 ± 0.05	15.99 ± 0.04	15.53 ± 0.04	15.81 ± 0.05	15.70 ± 0.05	15.85 ± 0.03
55809	2011-09-05	14.94 ± 0.04	15.57 ± 0.03	15.13 ± 0.04	15.39 ± 0.04	15.58 ± 0.04	15.78 ± 0.03

May 26 (MJD 52420), respectively. The spectral analysis was performed using the XSPEC v12.7 package.

Chandra Advanced CCD Imaging Spectrometer (ACIS)-S spectra and instrument responses were generated using the Chandra Interactive Analysis of Observations (CIAO) v4.3 and the related *Chandra* calibration data base. The 0.3–7 keV image shows the presence of an unresolved core, a diffuse halo, and a jet feature coincident with the inner radio/optical jet (see Birkinshaw et al. 2002).

The nuclear spectrum was extracted from an annular region ($r_{\rm in}$ = 0.3 arcsec, $r_{\rm out}$ = 1.2 arcsec) in order to minimize pile up effects.[6] The background counts were extracted from three source-free circular regions of r = 1.2 arcsec each. The 0.5–7 keV spectrum is well fitted (χ^2/dof = 187/199) by a PL absorbed by a column density slightly in excess of the Galactic value, $N_{\rm H} = (4.82 \pm 0.03) \times 10^{20}$ cm^{-2}.

The spectrum of the jet was extracted from a circle of radius 1 arcsec at a distance of 1.2 arcsec from the core. The background was chosen from three source-free circular regions. The best-fitting model is a PL with photon index $\Gamma_{\rm X} = 2.2 \pm 0.3$. The 2–10 keV flux of the jet is roughly 20 times lower than the core flux. *Chandra* spectral results for the nucleus and the jet are listed in Table 4.

The *XMM–Newton*-European Photon Imaging Camera (EPIC) observation of PKS 0521−36 was analysed using the Science Analysis System (SAS) v11.0 software and available calibration files. Time intervals affected by high background were excluded. After this data cleaning, we obtained a net exposure of 26.6 ks and a count rate of 3.50 ± 0.01 counts s^{-1} for the pn. The source and background spectra were extracted from circular regions of 32 and 44 arcsec radius, respectively. The response matrices were created using the SAS commands RMFGEN and ARFGEN. The nuclear data are not piled up. Data were grouped into 25 counts per bin in order to apply the χ^2 statistic. A PL, absorbed by Galactic column density, plus a thermal (APEC) component is a good parametrization of the data (χ^2/dof = 972/925). In Foschini et al. (2006), a broken PL model absorbed by the Galactic column was reported as the best fit to these *XMM–Newton* data. However the 0.5–10 keV best-fitting model turns out to be a combination of a broken PL, describing the nuclear radiation, plus a Raymond–Smith component (χ^2/dof = 947/923), which accounts for the thermal emission of the diffuse halo around the source, necessarily inside the 32 arcsec extraction radius. It is interesting to note that the two spectral indices of the broken PL are similar to those observed for the nucleus and the jet by *Chandra*. This may indicate that we are observing both these components in the *XMM–Newton* spectrum. An alternative possibility is that in the *XMM–Newton* spectrum we are observing the tail of the synchrotron emission and the rise of the inverse Compton (IC) component from the jet. There is no significant evidence for a Fe Kα emission line. *XMM–Newton* spectral results are listed in Table 5.

[6] Using the PIMMS software (http://cxc.harvard.edu/toolkit/pimms.jsp), the pile up for this source was estimated to be around 4 per cent.

Table 4. Spectral results of the nucleus and the jet of PKS 0521−36 for the *Chandra* observation performed on 1999 December 31. A PL model was used.

Component	Parameter	Value
Nucleus	$N_{\rm H}$ (cm^{-2})	$(4.82 \pm 0.03) \times 10^{20}$
	Γ	1.7 ± 0.1
	Norm (photons keV^{-1} cm^{-2} s^{-1})	$(3.1 \pm 0.4) \times 10^{-4}$
	$F_{2\text{-}10\,\rm keV}$ (erg cm^{-2} s^{-1})	$(1.3 \pm 0.2) \times 10^{-12}$
Jet	$N_{\rm H}$ (cm^{-2})	3.58×10^{20} (fixed)
	Γ	2.2 ± 0.3
	Norm (photons keV^{-1} cm^{-2} s^{-1})	$(2.4^{+1.2}_{-0.3}) \times 10^{-5}$
	$F_{2\text{-}10\,\rm keV}$ (erg cm^{-2} s^{-1})	$(6.0^{+3.0}_{-1.0}) \times 10^{-14}$

4 RADIO DATA

4.1 VLBA observations

PKS 0521−36 was observed with the VLBA at 8 and 15 GHz on 2003 January 7. The central frequencies of the two bands were 8.421 and 15.356 GHz and the total bandwidth was 32 MHz for each band. The on-source time was about 30 and 50 min at 8 and

Table 5. Spectral results for the *XMM–Newton* observation of PKS 0521−36 performed on 2002 May 26. A broken PL model with $N_{\rm H}$ fixed to the Galactic absorption plus a Raymond–Smith component was used.

Parameter	Value
Γ_1	2.4 ± 0.2
$E_{\rm b}$ (keV)	$0.76^{+0.07}_{-0.04}$
Γ_2	1.7 ± 0.2
Norm (photons keV^{-1} cm^{-2} s^{-1})	$(1.7 \pm 0.1) \times 10^{-3}$
kT (eV)	$0.85^{+0.09}_{-0.07}$
Norm (photons keV^{-1} cm^{-2} s^{-1})	$(8.2 \pm 2.7) \times 10^{-5}$
$F_{2\text{-}10\,\rm keV}$ (erg cm^{-2} s^{-1})	$(8.0 \pm 0.7) \times 10^{-12}$

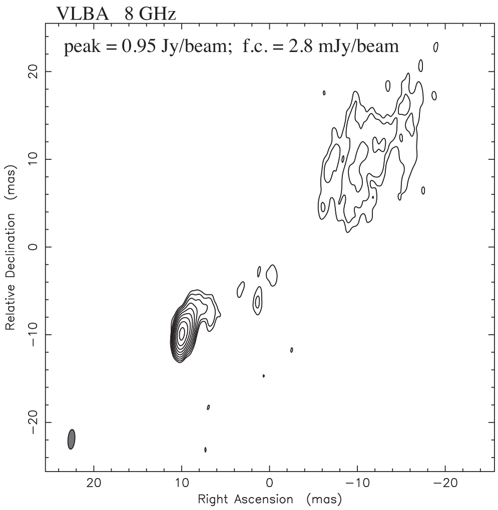

Figure 6. VLBA image of PKS 0521−36 at 8 GHz. On the image we provide the restoring beam, plotted in the bottom left-hand corner, the peak flux density in Jy beam^{-1}, and the first contour (f.c.) intensity in mJy beam^{-1}, which is three times the off-source noise level. Contour levels increase by a factor of 2.

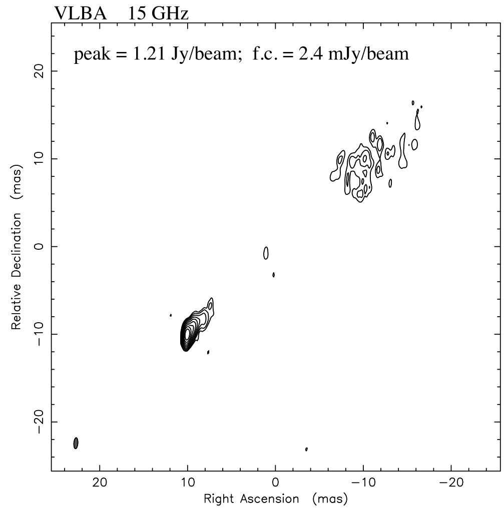

Figure 7. VLBA image of PKS 0521−36 at 15 GHz. On the image we provide the restoring beam, plotted in the bottom left-hand corner, the peak flux density in Jy beam^{-1}, and the first contour (f.c.) intensity in mJy beam^{-1}, which is three times the off-source noise level. Contour levels increase by a factor of 2.

15 GHz, respectively, divided into 10 scans distributed over a wide range of hour angle, to ensure the best sampling of the (u, v)-plane. One station (North Liberty) could not provide data, while two performed poorly because of snow (Hancock) and hardware problems (Brewster).

We downloaded the data from the National Radio Astronomy Observatory (NRAO) archive and performed the typical steps of calibration in the astronomical image processing system (AIPS). We used system temperature and gain curve tables for the visibility amplitude calibration and FRING for the delay, rate, and visibility phase. Uncertainties on the amplitude calibration are about 10 per cent. Several cycles of self-calibration were then performed in DIFMAP to improve the initial calibration, both in phase and amplitude, and produce final images.

In Figs 6 and 7, we show total intensity images of PKS 0521−36 at 8 and 15 GHz, respectively. The source is well detected at both frequencies, with a bright compact core and a one-sided jet oriented in PA $\sim -45°$ on the plane of the sky. The brightness profile along the jet axis decreases rapidly with increasing distance from the core, but it then suddenly rises again at ∼30 mas. The total flux density is 1.78 and 1.93 Jy at 8 and 15 GHz, respectively, with a peak brightness of 0.94 and 1.21 Jy beam^{-1}. The core has an inverted spectral index of $\alpha_{\rm r} = -0.4 \pm 0.2$ ($S(\nu) \propto \nu^{-\alpha_{\rm r}}$). The bright jet emission region at ∼30 mas has a flux density $S_8 \sim 405$ mJy and $S_{15} \sim 265$ mJy, corresponding to a spectral index of $\alpha_{\rm r} = 0.7 \pm 0.2$.

In Table 6, we report the parameters of a model fit with Gaussian components to the visibility plane. We have first model fitted the 8 GHz visibilities with δ (for the core), circular (for the inner jet), and elliptical (for the outer blob) Gaussian components, until we reached convergence. Then, we used this model as a starting condition for the model fit to the 15 GHz visibilities. In this latter fit, we kept the position and size of the outer three components fixed, while all the other parameters (including the flux density of every component) were left free to vary.

In order to maximize sensitivity to the diffuse jet emission, we also produced an image applying a Gaussian taper of 0.3 at a radius of 30 Mλ to the 8 GHz data set. This yields a resolution of 4.9 × 14.2 mas^2 in PA 2°.3, a peak brightness in the jet region of about 185 mJy beam^{-1}, and an off source peak of 1.4 mJy beam^{-1} on the counter-jet side.

4.2 VLA data

To obtain information on the radio flux density on kpc-scale, we retrieved archival NRAO VLA data at 4.9 and 8.4 GHz. Observations of PKS 0521−36 were performed at 4.9 GHz on 2009 August 6, when the array was in C configuration, while 8.4-GHz observations were carried out on 2009 October 3 when the array was in the hybrid C and D configuration. During both runs the target was observed for about 40 s. A few antennas did not participate in the observations due to a system upgrade. The primary flux density calibrator was 3C 48. Uncertainties on the amplitude calibration (1σ) are about 5 per cent at both frequencies. The data reduction was carried out following the standard procedures for the VLA implemented in the NRAO AIPS package. The flux density at each frequency was measured on the final image produced after a few phase-only self-calibration iterations using TVSTAT, which performs an aperture integration over a selected region on the image plane. Flux density of the compact components was measured by the AIPS task JMFIT, which performs a Gaussian fit of the source component on the image plane. Flux densities are reported in Table 7. The resolution

Table 6. Model-fit parameters. Columns (1) and (2): flux density S of the components; columns (3) and (4): the radial distance d from the core at 8 and 15 GHz, respectively; columns (5) and (6): the polar angle θ, measured north to east at 8 and 15 GHz, respectively; columns (7) and (8): the major axis a of the component (0 indicates a δ component); column (9): the ratio b/a between the minor and major axis of the component (1 indicates a circular Gaussian); column (10): the orientation ϕ of the major axis on the plane of the sky; column (11): the spectral index α_r. Numbers in italics refer to parameters held fixed in the model fit.

S_8 (mJy) (1)	S_{15} (mJy) (2)	d_8 (mas) (3)	d_{15} (mas) (4)	θ_8 (°) (5)	θ_{15} (°) (6)	a_8 (mas) (7)	a_{15} (mas) (8)	b/a (9)	ϕ (°) (10)	α_r (11)
545	815	0.00	0.00	0.0	0.0	0.00	0.00	*0*	0	−0.7
414	584	0.28	0.27	−54.9	−33.6	0.37	0.27	*1*	0	−0.6
233	195	0.96	0.96	−42.9	−43.0	0.44	0.25	*1*	0	0.3
100	72	2.06	2.28	−34.1	−42.8	0.87	1.11	*1*	0	0.5
33	12	4.30	4.35	−40.8	−39.9	1.18	*1.18*	*1*	0	1.7
38	25	10.8	*10.8*	−55.5	*−55.5*	4.58	*4.58*	*1*	0	0.7
298	220	27.9	*27.9*	−45.9	*−45.9*	7.95	*7.95*	0.58[a]	−19.7[a]	0.5
94	59	35.3	*35.3*	−47.3	*−47.3*	8.53	*8.53*	0.47[a]	−6.9[a]	0.8

[a]These values are left free to vary in the model fit at 8 GHz and fixed at 15 GHz.

Table 7. VLA flux density and spectral index of PKS 0521−36.

Comp	$S_{4.9}$ (Jy)	$S_{8.4}$ (Jy)	$\alpha_{4.9}^{8.4}$
C	3.72 ± 0.18	3.94 ± 0.20	–0.1 ± 0.1
S	2.18 ± 0.11	1.35 ± 0.07	1.0 ± 0.1
Ext	1.12 ± 0.06	0.35 ± 0.03	2.1 ± 0.2
Tot	7.02 ± 0.35	5.64 ± 0.28	0.4 ± 0.1

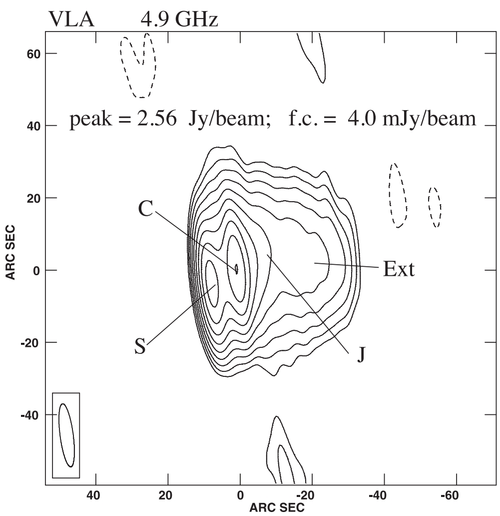

Figure 8. VLA image of PKS 0521−36 at 4.9 GHz. On the image we provide the restoring beam, plotted in the bottom left-hand corner, the peak flux density in Jy beam^{-1}, and the first contour (f.c.) intensity in mJy beam^{-1}, which is three times the off-source noise level. Contour levels increase by a factor of 2.

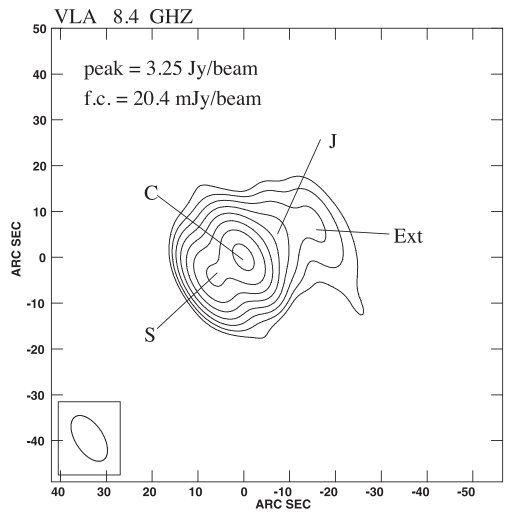

Figure 9. VLA image of PKS 0521−36 at 8.4 GHz. On the image we provide the restoring beam, plotted in the bottom left-hand corner, the peak flux density in Jy beam^{-1}, and the first contour (f.c.) intensity in mJy beam^{-1}, which is three times the off-source noise level. Contour levels increase by a factor of 2.

achieved is about 17 × 4 and 11 × 6 arcsec^2 at 4.9 and 8.4 GHz, respectively.

In Figs 8 and 9 we show the total intensity images at 4.9 and 8.4 GHz, respectively. The radio emission is dominated by two compact components, labelled C and S, whose flux density is about 80 and 73 per cent of the source total flux density at 4.9 and 8.4 GHz, respectively. The central component, coincident with the optical nucleus, has an inverted spectrum ($\alpha_{4.9}^{8.4} \sim$ –0.1 ± 0.1) and hosts the source core. This value is larger than that derived from VLBA data and this is likely due to the contribution of the jet that cannot be separated from the core component due to the lower resolution of the VLA observations. A jet-like structure, labelled J, emerges from the core with a position angle of about −45°, in agreement with what is found in high-resolution VLBA images (Fig. 7). At about 5 arcsec (5 kpc) from the core, the jet bends towards the west, producing an extended structure of about 30 arcsec (∼30 kpc) in size, in agreement with what is found at lower frequencies (Ekers et al. 1989; Falomo et al. 2009). Component S is located about 7 arcsec (∼7 kpc) from the central component with a position angle of 120° and it marks the location of the hotspot. Its spectral index is rather steep $\alpha_{4.9}^{8.4} = 1.0 \pm 0.1$ and it is likely due to the low resolution of these observations, which does not allow us to disentangle the contribution of the hotspot from that of the lobe. It is worth noting

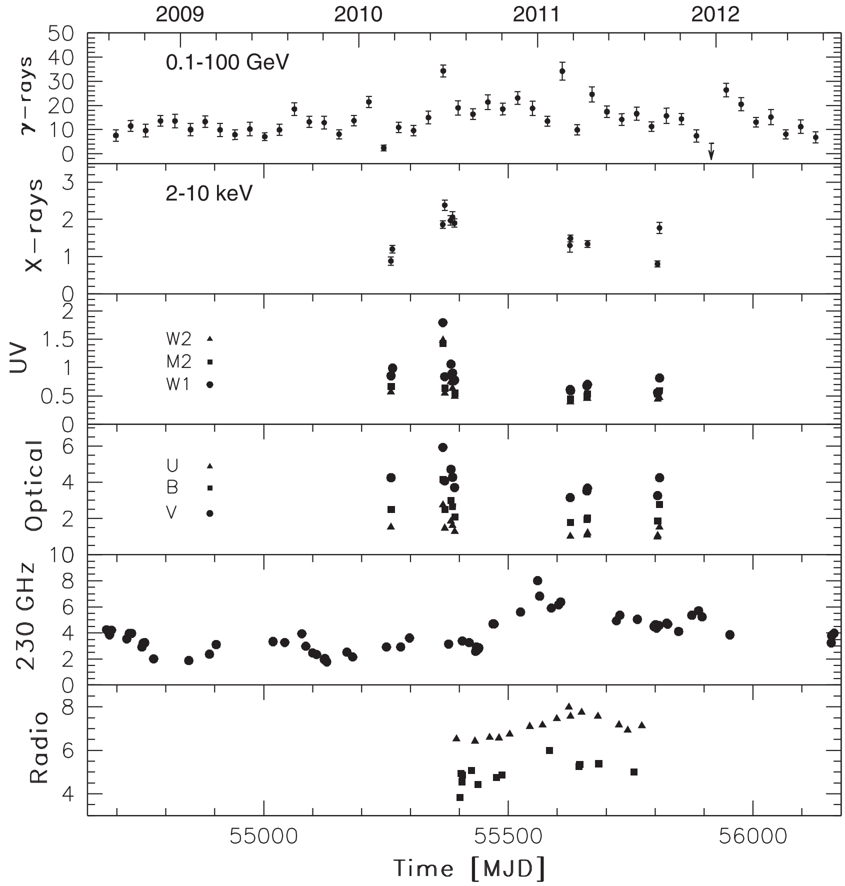

Figure 10. Multifrequency light curve for PKS 0521−36. The period covered is 2008 August 4–2012 August 4 (MJD 54682–56143). The data were collected (from top to bottom) by *Fermi*-LAT (γ-rays; in units of 10^{-8} photons cm^{-2} s^{-1}), *Swift*-XRT (X-rays; in units of 10^{-11} erg cm^{-2} s^{-1}), *Swift*-UVOT ($w1$, $m2$, and $w2$ filters; in mJy), (v, b, and u filters; in mJy), SMA (230 GHz; in Jy), UMRAO (8 and 15 GHz, triangles and squares, respectively; in Jy). The LAT data were obtained with the photon index left free to vary (see Fig. 3).

that the spectral indices have been computed assuming the total flux density measured on images with different resolution, which may produce an artificial steepening of the spectrum. The errors on the spectral index have been computed by means of the error propagation theory.

4.3 UMRAO data

UMRAO centimetre band total flux density observations were obtained with the University of Michigan 26-m paraboloid located in Dexter, Michigan, USA. The instrument is equipped with transistor-based radiometers operating at frequencies centred at 4.8, 8.0, and 14.5 GHz with bandwidths of 0.68, 0.79, and 1.68 GHz, respectively. Dual horn feed systems are used at 8 and 14.5 GHz. Each observation consisted of a series of 8–16 individual measurements over approximately a 25–45 min time period, utilizing an ON–ON technique (switching the target source between the two feed horns which are closely spaced on the sky) at 8.0 and 14.5 GHz. As part of the observing procedure, drift scans were made across strong sources to verify the telescope pointing correction curves, and observations of nearby calibrators were obtained every 1–2 h to correct for temporal changes in the antenna aperture efficiency. Further details about UMRAO are reported in Aller et al. (2014). UMRAO data at 8 and 14.5 GHz are represented in Fig. 10.

4.4 SMA data

The 230 GHz (1.3 mm) light curve was obtained at the SMA on Mauna Kea (Hawaii). PKS 0521−36 is a bright AGN included in an ongoing monitoring program at the SMA to determine the fluxes of compact extragalactic radio sources that can be used as calibrators at mm wavelengths. Details of the observations and data reduction can be found in Gurwell et al. (2007). Data from this programme are updated regularly and are available at the SMA website.[7] SMA data at 230 GHz are shown in Fig. 10.

5 DISCUSSION

5.1 Identification of the γ-ray source

The association of a γ-ray source with a low-energy counterpart is fundamental for understanding its physical properties. The accuracy with which most of the γ-ray sources were localized with EGRET was not enough to associate them with a known counterpart, leaving the legacy of a large fraction of unidentified sources in γ-rays. Thanks to larger photon statistics and unprecedented angular resolution at high energies *Fermi*-LAT is able to investigate the natures and counterparts of these unidentified sources, although the

[7] http://sma1.sma.hawaii.edu/callist/callist.html. Use in publication requires obtaining permission in advance.

γ-ray activity state as well as correlated flux variability at different frequencies play an important role for the identification process of a γ-ray source (e.g. D'Ammando et al. 2012).

A γ-ray source at a position compatible with PKS 0521−36 was detected with a 4.3σ significance by EGRET during 1992 May 14–June 4, with a flux of (1.8 ± 0.5) × 10^{-7} photons cm^{-2} s^{-1} and a photon index $\Gamma_\gamma = 2.16 \pm 0.36$ (Lin et al. 1995). As a result of that activity the source was included in the Second EGRET catalogue as 2EG J0524−3630 (Thompson et al. 1995). The γ-ray source 3EG J0530−3626 was included in the Third EGRET catalogue, but PKS 0521−36 was outside the 99 per cent confidence contour in that catalogue, and the association between the γ-ray source and the AGN was not confirmed (Hartman et al. 1999). The same conclusion was drawn for the γ-ray source EGR J0529−3608 reported in the revised EGRET catalogue proposed by Casandjian & Grenier (2008).

No γ-ray source associated with PKS 0521−36 was reported in the LAT Bright Source List obtained after the first three months of *Fermi* operation (Abdo et al. 2009b), but the AGN was associated with 1FGL J0522.8−3632, 2FGL J0523.0−3628, and 3FGL J0522.9−3628 in the following *Fermi* catalogues (Abdo et al. 2010c; Nolan et al. 2012; Acero et al. 2015).

Most of the associations of γ-ray sources with AGN in the *Fermi* catalogues have high probability of being true, but a firm identification needs to be confirmed by means of correlated variability in different energy bands. The contemporaneous increase of activity observed in the optical, UV, X-ray, and γ-ray bands in 2010 June (Fig. 10) is a distinctive signature for the identification of the γ-ray source with PKS 0521−36. In the following, we investigate the properties of PKS 0521−36 from radio to γ-ray energy bands with the goal of unveiling the nature of this γ-ray emitting AGN.

5.2 Gamma-ray properties

By comparing the γ-ray properties of PKS 0521−36 with those of the different types of AGN detected by LAT, we noted that the average photon index of this source ($\Gamma_\gamma = 2.45 \pm 0.02$) is similar to the average value observed for FSRQ ($\Gamma_\gamma = 2.44 \pm 0.20$; Ackermann et al. 2015) and misaligned AGN ($\Gamma_\gamma = 2.42 \pm 0.28$; Abdo et al. 2010b). As shown in Fig. 3, there is no general trend between γ-ray flux and photon index for PKS 0521−36, but a significant hardening of the spectrum was observed during the γ-ray flaring activity in 2010 June. This behaviour is in common with bright FSRQ and low-synchrotron-peaked BL Lacs detected by LAT (Abdo et al. 2010b). The hardening of the spectrum together with the low redshift make this source a promising target for the current (i.e. MAGIC, VERITAS, and HESS) and next generation of imaging atmospheric Cherenkov telescopes (e.g. the Cherenkov Telescope Array). It is interesting to note that one of the few radio galaxies detected at Very High Energy (VHE; $E > 100$ GeV), NGC 1275 (Aleksić et al. 2012), showed flux and spectral index similar to those of PKS 0521−36 during the 2010 June flare.

Contrary to the photon index, the average apparent isotropic γ-ray luminosity of PKS 0521−36 ($L_\gamma = 5.2 \times 10^{44}$ erg s^{-1}) seems to lie in the region usually occupied by BL Lacs and radio galaxies (Ackermann et al. 2015). However, the lower apparent luminosity of PKS 0521−36 with respect to both FSRQ and the steep spectrum radio quasars (SSRQ) 3C 380 and 3C 207 may be due to the close proximity of the source. In fact, a γ-ray flaring activity with peak flux of 1–2 × 10^{-6} photons cm^{-2} s^{-1}, as observed for PKS 0521−36, is quite uncommon in BL Lacs (e.g. Cannon 2010) and in misaligned AGN, the only exception being the radio galaxy NGC 1275 (e.g. Ciprini 2013).

It is not clear whether the most powerful jets of the two parent populations (FSRQ and FR II radio galaxies) have analogous structures. The difference in the jet structure may be related to the different environment or to jet properties. We noted that the FR II radio galaxy Cygnus A, one of the most powerful radio sources with a redshift comparable to that of PKS 0521−36, has not been detected in γ-rays so far. On the other hand, Pictor A, an FR II radio galaxy at redshift $z = 0.035$, was detected by *Fermi*-LAT (Acero et al. 2015), but with an apparent γ-ray luminosity that is two order of magnitudes lower than that observed for PKS 0521−36. This may support the scenario of a complex jet structure in radio galaxies (e.g. velocity gradients, spine layer) with possible differences in the emission mechanisms at higher energies also among objects of the same class. Alternatively, the different viewing angle with respect to the observer, and thus the different Doppler boosting of the jet emission, may lead to the detection or not of radio galaxies in γ-rays.

No significant difference was observed between the average γ-ray flux detected by EGRET in 1992 and LAT during 2008–2012. This is different from the long-term variability observed for the radio galaxy NGC 1275 between the EGRET and *Fermi* era. In that case, the early LAT observations revealed a flux at least seven times higher than the upper limit obtained by EGRET (Kataoka et al. 2010). Of particular interest is the short variability observed during flaring periods with a doubling time-scale of the order of a few hours, compatible with the variability observed in some bright FSRQ (e.g. Abdo et al. 2010a; Tavecchio et al. 2010; Saito et al. 2013). If the emitting region fills the entire cross-section of the jet, this rapid variability suggests a compact γ-ray emitting region and the location of the γ-ray emission may be within the broad-line region (BLR). Following the causality argument and considering the 12-h variability observed during the γ-ray flares the size of the emitting region should be $R < ct_{\rm var}\delta/(1 + z) = 6.3 \times 10^{15}$ cm (assuming $\delta = 5$; see Section 5.5). This size is smaller than the values usually inferred from the SED modelling of blazars within the framework of the standard one-zone leptonic model (e.g. Ghisellini et al. 2011). Alternatively, episodes of fast variability can be produced in a jets-within-jet/minijets scenario (e.g. Ghisellini & Tavecchio 2008; Giannios, Uzdensky & Begelman 2009) and in this case the location may be further out, as proposed e.g. for M87 (e.g. Giroletti et al. 2012), or produced by turbulent cells in the relativistic plasma (Marscher 2014).

5.3 Radio properties

On a kpc scale, the radio source shows a two-sided structure where jets, lobes, and a hotspot are clearly visible in addition to the core. The structure revealed by the VLBA images agrees with those reported in previous works (e.g. Tingay & Edwards 2002; Giroletti et al. 2004). However, since the data were taken at distant epochs and at different frequencies, it is difficult to make a reliable identification of the individual components. The best possible match is probably on the bright diffuse region at ∼30 mas, whose flux density and position are consistent in the various data sets, and essentially stationary within the uncertainty related to its large size (∼8 mas). This bright resolved structure is reminiscent of two other γ-ray emitting AGN somewhat different from the typical blazars, i.e. M87 (Abdo et al. 2009a) and 3C 120 (Abdo et al. 2010b; Kataoka et al. 2011). On parsec scales, both sources show a one-sided jet whose brightness profile along the axis initially decreases down to the noise level and then steeply rises in an extended, stationary feature. The projected distance of this feature is ∼50 pc in 3C 120 (Roca-Sogorb et al. 2010) and ∼70 pc in M87 (Cheung, Harris & Stawarz 2007; Giroletti et al. 2012). In PKS 0521−36, a bright, extended jet feature is found at nearly 30 pc (projected). These features may be interpreted as recollimation shocks, and at least in the case of M87 it has been proposed that high-energy emission up to the TeV regime might originate at this location (Bromberg & Levinson 2009). Recently, a similar scenario was suggested also for the rapid VHE flaring activity of the FSRQ 4C 21.35 (Tavecchio et al. 2011), although different models are proposed (Dermer, Murase & Takami 2012; Tavecchio et al. 2012; Ackermann et al. 2014).

We estimated the ranges of viewing angles θ and jet velocity β ($=v/c$) from the jet/counter-jet brightness ratio from the radio images presented in Section 4.1. Assuming the off-nuclear peak on the counter-jet side as an upper limit to any possible counter-jet brightness, we calculate a jet/counter-jet brightness ratio $R \sim 130$. In the standard hypothesis that jet and counter-jet are intrinsically similar and that any asymmetry is entirely due to relativistic beaming, this places limits on the jet velocity and orientation by

$$R = \frac{B_{\rm j}}{B_{\rm cj}} = \left(\frac{1+\beta\cos\theta}{1-\beta\cos\theta}\right)^{2+\alpha_{\rm r}}, \tag{1}$$

and we obtain $\beta > 0.75$, $\delta > 1.5$, $\theta < 41°$, assuming $\alpha_{\rm r} = 0.7$.

The radio spectrum below 1 GHz is dominated by the flux density arising from the extended structures. The spectral index computed between 160 MHz (Slee 1977) and 1.4 GHz from the NRAO VLA Sky Survey (Condon et al. 1998) results to be 0.7. This radio spectral shape and the optical emission suggest that PKS 0521−36 may be an intermediate object between a broad-line radio galaxy (BLRG) and an SSRQ.

We computed the core dominance (CD) of PKS 0521−36 following the definition in Orr & Browne (1982) and Abdo et al. (2010b):

$$\mathrm{CD} = \frac{S_{\rm core}}{S_{\rm tot} - S_{\rm core}}, \tag{2}$$

where the core flux density $S_{\rm core}$ and the total flux density $S_{\rm tot}$ refer to the source rest frame ($S = S_{\rm obs}(1+z)^{\alpha_{\rm r}-1}$). For the core flux density we consider the value measured on the VLA image at 4.9 GHz and reported in Table 6, and we assume a flat spectrum $\alpha_{\rm r} = 0$. In order to prevent missing flux density associated with extended emission, we consider the total flux density measured by the Parkes telescope at 5 GHz, which is $S_{\rm tot} = 8.1$ Jy (Wright et al. 1996), and we assume a spectral index $\alpha_{\rm r} = 0.7$. We obtain log(CD) = −0.10. This value is similar to those shown by the γ-ray emitting SSRQ 3C 380 and 3C 207 and BLRG 3C 111 (Abdo et al. 2010b).

In order to estimate the radio power and to make a comparison with the γ-ray emitting misaligned AGN, we computed the radio luminosity at 178 MHz by using

$$L = 4\pi d_L^2 S (1+z)^{\alpha_{\rm r}-1}, \tag{3}$$

where d_L is the luminosity distance, and S is the flux density at 178 MHz, which has been extrapolated from the values reported in the literature and corresponds to 67.5 Jy (source rest frame). The corresponding luminosity is $L = 4.8 \times 10^{26}$ W Hz^{-1}, which is a few orders of magnitude lower than the luminosity of the SSRQ 3C 380 and 3C 207, but is comparable with the luminosity of the BLRG 3C 111.

5.4 X-ray to mm behaviour

During 2005–2011 the source was monitored by the *Swift* satellite only sporadically, but a quite prominent flare was observed from optical to X-rays in 2010 June, contemporaneous with the peak of γ-ray flaring activity (see Section 5.1). The small variability amplitude (calculated as the ratio of maximum to minimum flux) observed in X-rays (∼3) with respect to that observed in γ-rays (∼13 on a monthly time-scale up to a factor of ∼50 on a daily time-scale) together with the lack of hardening of the spectrum may be an indication that the X-ray emission is produced by the low-energy tail of the same electron distribution, as observed in FSRQ (e.g. PKS 1510−089; D'Ammando et al. 2011). On a time-scale of years a change by a factor of ∼10 in flux was detected between the *Chandra* and *Swift* observations. A second less prominent increase of the X-ray activity was observed on 2011 September 5, with no evident counterpart in γ-rays. This may be due to different mechanisms or emission sites that give significant contribution in X-rays and γ-rays in that period. The photon indices observed by *Swift*-BAT and *Swift*-XRT in hard X-rays ($\Gamma_{\rm X} \sim 1.8$) and soft X-rays ($\Gamma_{\rm X} \sim 1.7$) indicate that the peak of the IC emission should be at MeV energies, according to the spectra observed by *Fermi*-LAT ($\Gamma_\gamma > 2$).

The variability amplitude in the optical–UV bands covered by *Swift*-UVOT is $v \sim 1.9$, $b \sim 2.4$, $u \sim 2.9$, $w1 \sim 3.2$, $m2 \sim 3.2$, and $w2 \sim 3.7$. We observed a larger variability amplitude at higher frequencies, contrary to what is observed in quasars, where the contribution from the thermal accretion disc significantly increases in the UV part of the spectrum, diluting the jet emission (e.g. Raiteri et al. 2012). This suggests the lack of a prominent accretion disc in the broad-band spectrum of the source. We noted that during the flaring activity in 2010 June the optical and UV emission seems to peak a few days before the X-ray peak. This may be due the coverage provided by the *Swift* observations, and thus the lack of an observation at the time of the daily γ-ray peak, or to the complex jet structure with different parts of the jet responsible for the emission at different frequencies.

The SMA data at 230 GHz show an amplitude variability of ∼4, with a peak flux density of 8 Jy on 2010 December 30 (MJD 55560). This event at millimetre wavelengths may be the delayed flare with respect to the γ-ray flare observed in 2010 June. The increase of flux density was observed also by UMRAO at 15 and 8 GHz, with the difference in time of about 1 and 2 months, respectively, with respect to the 230 GHz emission likely related to opacity effects due to synchrotron self-absorption. Recently, Fuhrmann et al. (2014) investigated the correlation between radio and γ-ray emission for a sample of bright *Fermi* blazars. Performing a stacking analysis of the objects in the sample, they found at 142 GHz a time-lag of (7 ± 9) d between the radio and γ-ray emission, with the γ-ray leading the radio emission. In this context a delay of 6 months between the peak at 230 GHz and the γ-ray one for PKS 0521−36 is extremely large and thus unlikely, opening alternative scenarios. The emitting region responsible for the optical-to-γ-ray emission may be different from the region producing the mm and radio emission. However, we note that SMA data are not available in 2010 May–June, and therefore we cannot rule out an mm flare in the same period of the γ-ray flare.

5.5 SED modelling

We build two SED for PKS 0521−36 in two different activity states: the high state in 2010 June and a low state in 2010 February–March. The flaring SED includes the *Fermi*-LAT spectrum built with data centred on 2010 June 22–July 5 (MJD 55369–55382), the optical, UV, and X-ray data collected by *Swift* on 2010 June 23 (MJD 55370), and 230 GHz data collected by SMA on 2010 July 1 (MJD 55378). The low SED includes the LAT spectrum built with data centred on 2010 February 1–March 31 (MJD 55228–55286), the optical, UV, and X-ray data collected by *Swift* on 2010 March 5 (MJD 55260), and 230 GHz data collected by SMA on 2010 February 24 (MJD 55251).

The modelling of the SED of PKS 0521−36 within the framework of the standard one-zone leptonic model provides results at odds with the bulk of the blazar population. In particular, a quite low Doppler factor is required ($\delta \simeq 3$; e.g. Pian et al. 1996; Ghisellini et al. 2011), implying a relatively large viewing angle $\theta_{\rm v} \gtrsim 15^{\circ}$ and a low bulk Lorentz factor. This result can be traced back to the relatively small separation between the two bumps in the SED. This conclusion is corroborated by several hints, such as the existence of a large-scale optical jet and the moderate core-to-extended radio flux ratio. In the case of a relatively large viewing angle and thus small beaming amplification, it is not excluded that also slow regions of the jets contribute to the observed emission. This would be the case in the framework of the *structured jet* scenario, in which the flow is supposed to be composed of a fast inner core – or spine – surrounded by slower plasma – the layer (Ghisellini, Tavecchio & Chiaberge 2005; Tavecchio & Ghisellini 2008). Indeed such a scheme has been applied to interpret the emission of γ-ray emitting radio galaxies, for which the emission can be interpreted as a mix of spine and layer components (see also Tavecchio & Ghisellini 2014). With this motivation, in the following we focus our attention on the application of the structured jet model to the emission of PKS 0521−36.

We briefly recall the main features and the parameters of the model (refer to Ghisellini et al. 2005; Tavecchio & Ghisellini 2008, 2014 for a more complete description). The spine is assumed to be a cylinder with height $H_{\rm s}$ and radius $R_{\rm s}$ (the subscripts 's' and 'l' stand for spine and layer, respectively). The layer is modelled as a hollow cylinder with height $H_{\rm l}$, internal radius $R_{\rm s}$, and external radius $R_{\rm l} = 1.2 \times R_{\rm s}$. We assume $H_{\rm s} \ll H_{\rm l}$, ideally corresponding to the case of a perturbation travelling down the spine, surrounded by a relatively long and stationary layer of slow plasma.

In both zones we assume a phenomenological and stationary electron energy distribution described as a broken PL with the following parameters: minimum, maximum, and break Lorentz factors $\gamma_{\rm min}$, $\gamma_{\rm max}$, and $\gamma_{\rm b}$ and indices n_1 and n_2. The normalization of the electron distribution is parametrized by the emitted synchrotron luminosity, $L_{\rm syn}$. The emitting regions contain a tangled magnetic field $B_{\rm s}$, $B_{\rm l}$. The relativistic beaming is specified by the two Lorentz factors $\Gamma_{\rm s}$, $\Gamma_{\rm l}$ and by the viewing angle $\theta_{\rm v}$.

Electrons emit through synchrotron and IC mechanisms. Following Ghisellini & Tavecchio (2009), $R_{\rm BLR} = 10^{17} \times L_{\rm disc,45}^{0.5}$ cm and for $L_{\rm disc} = 3 \times 10^{43}$ erg s^{-1} we obtain $R_{\rm BLR} = 2 \times 10^{16}$ cm. Therefore the emitting region should be beyond the BLR and for this reason the external Compton of the BLR seed photons should be negligible. For the IC besides the local synchrotron radiation field (synchrotron self-Compton, SSC) we consider the beamed radiation field of the other component. Indeed, because of the relative motion, the energy density of radiation produced in one component is boosted by the square of the relative Lorentz factor $\Gamma_{\rm rel}$ in the rest frame of the other, where $\Gamma_{\rm rel} = \Gamma_{\rm s}\Gamma_{\rm l}(1 - \beta_{\rm s}\beta_{\rm l})$. As we will see, absorption of γ-rays through the interaction with the soft radiation field, $\gamma\gamma \rightarrow e^+e^-$ can be important. In the case under study, radiation is produced and absorbed within the same region and thus the

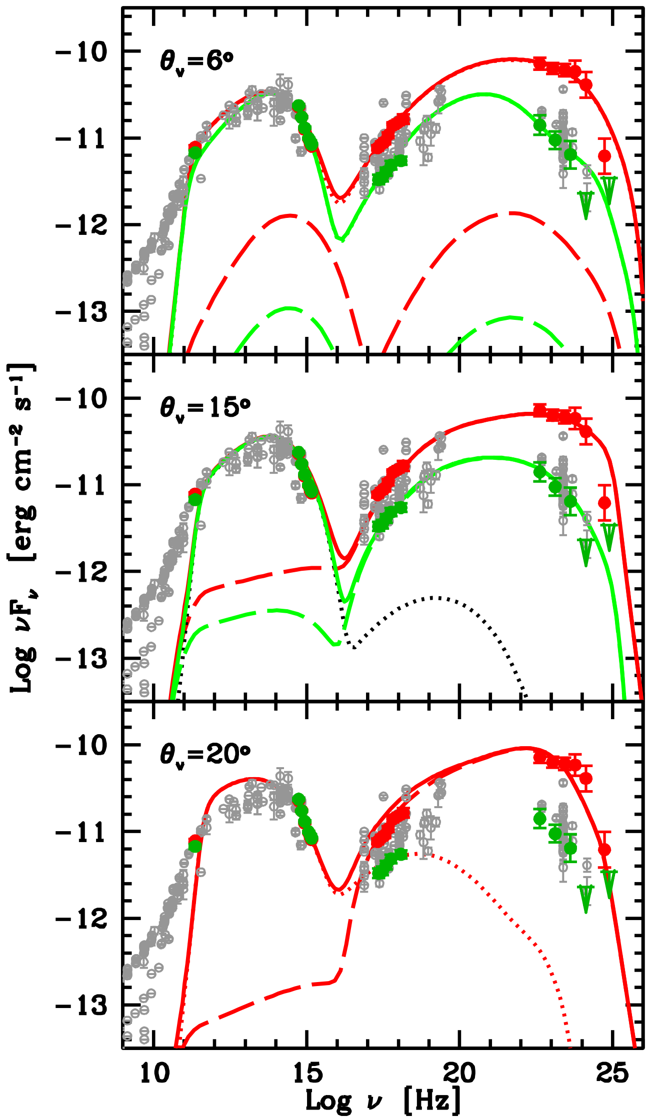

Figure 11. SED of PKS 0521−36. Red symbols show the high state, green symbols the low state. Arrows represent 2σ upper limits. Historical data (grey) are from the ASDC archive (http://tools.asdc.asi.it). The three panels report the results obtained with the structured jet emission model for different values of the viewing angle, from top to bottom: $\theta_{\rm v} = 6^{\rm o}$, 15°, and 20°. The dashed and the dotted lines show the emission from the layer and the spine, respectively. The thick solid line shows the total. For the case $\theta_{\rm v} = 15^{\rm o}$ the same spine emission (shown in black) is used for both states. See text for details.

'suppression factor' is $I(\nu)/I_{\rm o}(\nu) = (1 - \exp[-\tau_{\gamma\gamma}(\nu)])/\tau_{\gamma\gamma}(\nu)$ which, for large optical depths, is well approximated by $1/\tau_{\gamma\gamma}$.

We note that the number of the parameters is large (almost twice that of the simple SSC model). However, the model has to satisfy constraints that can be used as guidelines in selecting the suitable set-up. We refer to Tavecchio & Ghisellini (2014) for a detailed discussion.

Following the indications recalled in the previous subsections we consider angles larger than those usually associated with blazar jets, $\theta_{\rm v} \lesssim 5^{\circ}$. In Fig. 11 we show the results of the modelling of the SED with three different angles, $\theta_{\rm v} = 6^{\circ}$, 15°, and 20°. The corresponding parameters are reported in Table 8.

We expect that, for relatively small angles, the spine radiation is much more boosted than that of the layer, implying that the spine

Table 8. Input parameters of the models for the layer and the spine shown in Fig. 11. All quantities (except the bulk Lorentz factors Γ and the viewing angle θ_v) are measured in the rest frame of the emitting plasma. The external radius of the layer is fixed to the value $R_2 = 1.2R$.

	R (cm)	H (cm)	L_{syn} (erg $^{-1}$)	B (G)	γ_{min}	γ_b	γ_{max}	n_1	n_2	Γ	θ_v (°)
Layer low	3.5×10^{16}	2×10^{16}	6×10^{39}	0.5	100	3×10^3	7×10^4	1.5	3	3	6
Spine low	3.5×10^{16}	10^{15}	1.9×10^{41}	0.18	60	1.2×10^4	2.55×10^4	2	3.7	12	6
Layer high	3.5×10^{16}	2×10^{16}	7×10^{40}	0.5	100	3×10^3	7×10^4	1.5	3	3	6
Spine high	3.5×10^{16}	10^{15}	2.2×10^{41}	0.17	60	6×10^3	3×10^4	2.1	3	12	6
Layer low	5×10^{16}	2×10^{16}	1.3×10^{41}	1	80	3×10^4	10^5	2.75	4	3	15
Layer high	5×10^{16}	2×10^{16}	5.0×10^{41}	1	100	10^4	5×10^5	2.7	4	3	15
Spine[a]	5×10^{16}	10^{15}	4×10^{43}	15	10	2×10^3	6×10^3	2.1	3	10	15
Layer high	5×10^{16}	2×10^{16}	2×10^{41}	1	80	6×10^4	8×10^6	2.7	4	3	20
Spine high	5×10^{16}	10^{15}	4×10^{44}	15	10	300	8×10^3	2.1	3	10	20

[a]For the case $\theta_v = 15°$ the same spine emission has been used for both states.

emission component largely dominates the observed SED. This solution is that assumed for the case $\theta_v = 6°$ (upper panel). The relative stability of the low-energy component accompanied by the variation which occurred in the IC peak is obtained by changing the layer luminosity (and maintaining almost the same parameters for the spine). In fact, the spine IC bump is dominated in the high state by the component resulting from the IC scattering of the electrons in the spine with the photons coming from the layer. Variations of the layer luminosity are thus accompanied by substantial variations of the IC luminosity of the spine.

For larger angles the only suitable solution is that the two bumps are dominated by the two jet components, i.e. the low energy bump by the synchrotron component of the spine and the high energy bump by the IC emission of the layer (see the discussion in Tavecchio & Ghisellini 2014). For $\theta_v = 15°$ (middle panel) the model still reproduces quite well the data. In this case we also assume a stationary spine and a variable layer component. A further increase of the angle (lower panel) is limited by a problem already discussed in Tavecchio & Ghisellini (2014). Indeed, to compensate the reduced relativistic amplification of the spine emission one has to increase its intrinsic luminosity. This radiation field – concentrated in the optical–IR band – is the ideal target for the pair producing reactions $\gamma\gamma \rightarrow e^+ + e^-$ with γ-ray photons produced in the layer. In Fig. 12, we show the optical depth $\tau_{\gamma\gamma}$ and the corresponding 'suppression factor' $[1 - \exp(-\tau_{\gamma\gamma})]/\tau_{\gamma\gamma}$ as a function of the frequency for the case $\theta_v = 15°$ and 20°. The shapes of the curves, related to the spine target photon spectrum, are similar. However, due to the larger intrinsic luminosity, for $\theta_v = 20°$ the optical depth is larger by a factor of ≈10. As a consequence, while $\theta_v = 15°$ the source is transparent ($\tau_{\gamma\gamma} < 1$ up to ∼20 GeV, corresponding to the highest energy LAT bin in the high state, energy marked by the vertical yellow line), for $\theta_v = 20°$, the optical depth reaches unity already at ≈1 GeV and rapidly increases, determining the abrupt cut-off visible in Fig. 11 (lower panel). We therefore conclude that, in the framework of the structured jet model, the angle cannot be larger than about 15°.

In the unification scheme for radio galaxies and blazars we expect that, once observed at small angles, the SED of a radio galaxy resembles that of a typical blazar. Therefore for the remaining two cases, $\theta_v = 6°$ and 15°, one can further ask what kind of SED would the source present if observed at angles more typical for blazars. This is shown in Fig. 13, in which we report the SED as recorded by an observer at $\theta_v = 4°$, not changing the other parameters. For comparison we also display the historical SED of BL Lac. The

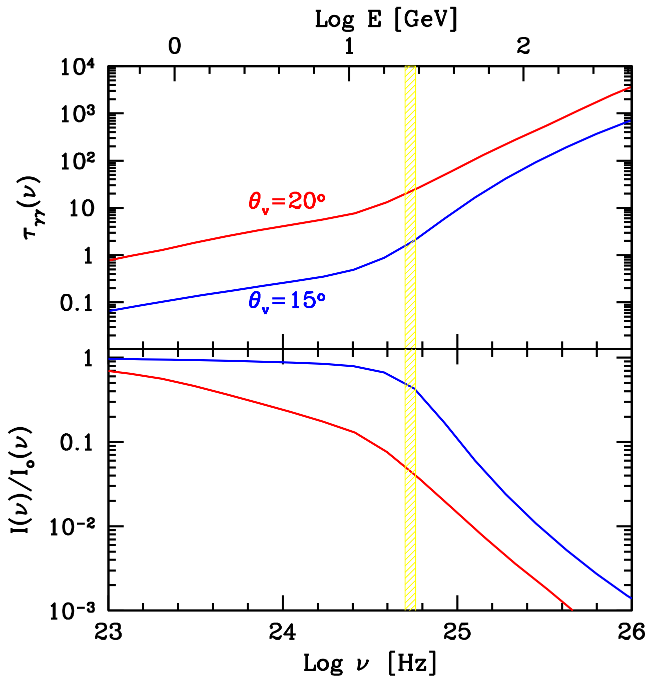

Figure 12. Optical depth (upper panel) and suppression factor (lower panel) for absorption of γ-rays within the jet as a function of the frequency for the models of the high states reported in Fig. 11, for $\theta_v = 15°$ (blue) and 20° (red). The vertical yellow line shows the upper energy limit of the LAT spectrum.

case $\theta_v = 15°$ (green) results in an SED strongly unbalanced (by a factor of ≈100) towards the synchrotron luminosity, at odds with the typical blazar SED. This effect is clearly related to the fact that the high-energy bump in the case $\theta_v = 15°$ is associated with the layer. At small angles, the layer radiation is much less beamed than that of the spine and this determines the substantial prominence of the low-energy peak. On the contrary, the SED for case $\theta_v = 6°$ (red) resembles that of the prototypical BL Lac. This suggests that a viewing angle between 6° and 15° is favoured.

In addition in the spine-layer scenario proposed here, the fast variability observed in γ-rays is difficult to reconcile with the cases that have $\theta_v = 15°$, in which the region responsible for the γ-ray emission is relatively large (5×10^{16} cm) and the Doppler factor

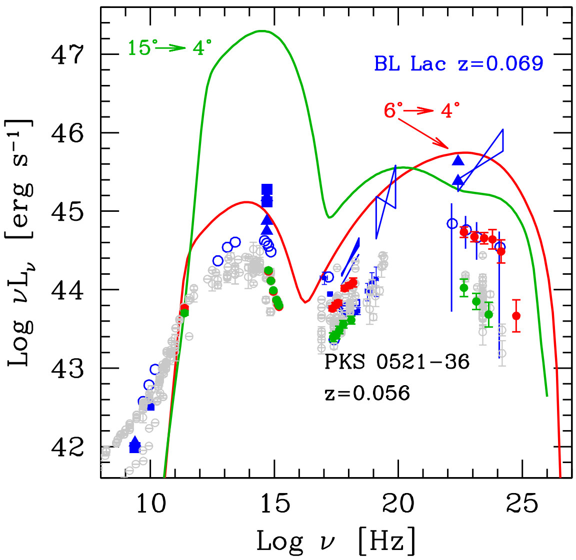

Figure 13. The green and the red lines show the emission from the spine-layer model of PKS 0521−36 for the cases $\theta_v = 15°$ and $6°$ as observed at $\theta_v = 4°$. Red symbols show the high state, green symbols the low state. LAT upper limits are not shown. For comparison, the blue data points describe the SED of BL Lac itself.

small ($\delta = 4$). Reducing the size of the emitting region in these two cases should lead to an increase of the compactness of the region and thus of the corresponding γ-ray opacity. This is another indication in favour of a relatively small viewing angle.

However, we cannot rule out the possibility that PKS 0521−36 is an AGN seen at $\theta_v \sim 15°$ and its 'aligned' counterpart is a blazar belonging to a population of synchrotron-dominated objects.

6 CONCLUSIONS

We investigated the properties of PKS 0521−36, an AGN with uncertain classification. We report results on multiwavelength observations of this source obtained from radio through γ-rays by SMA, UMRAO, VLA, *Swift*, and *Fermi*-LAT, mostly during 2008 August–2012 August. In addition archival *XMM–Newton*, *Chandra*, and VLBA observations were analysed.

The historical classification of this source as a BL Lac object is in contrast with the broad emission lines observed in optical and UV, with EW larger than 5 Å (rest frame). The presence of broad emission lines may suggest a classification as an FSRQ, but the radio spectrum below 1.4 GHz is not flat ($\alpha_r \sim 0.7$). The radio spectral shape and the optical emission lines indicate a possible classification as an intermediate object between BLRG and SSRQ. On pc-scales PKS 0521−36 shows a one-sided jet with a brightness distribution along the axis decreasing down to the noise level and then rising in an extended, stationary feature at nearly 30 pc. This is similar to what was observed in M87 and 3C 120, two γ-ray emitting misaligned AGN. The core dominance estimated for PKS 0521−36 is similar to those of the γ-ray emitting SSRQ 3C 380 and 3C 207 and BLRG 3C 111, suggesting an intermediate viewing angle with respect to the observer.

The fit of the *XMM–Newton* EPIC-pn spectrum confirmed the presence of a contribution of the thermal component identified by Birkinshaw et al. (2002) in the *Chandra* image as a diffuse halo around the AGN. No significant Fe Kα emission was detected in the *XMM–Newton* spectrum. This seems to disagree with the possible classification of PKS 0521−36 as a BLRG, although a smaller viewing angle with respect to the other BLRG may lead to a significant increase of the jet component that overwhelms the Fe Kα line in this object (similarly to the case of the narrow-line Seyfert 1 galaxy PMN J0948+0022; D'Ammando et al. 2014).

The contemporaneous flux increase observed from optical to γ-rays during 2010 June suggests the identification of the γ-ray source with PKS 0521−36. The 230 GHz light curve showed an increase of activity peaking on 2011 January. A delay of ~6 months between the emission at mm and γ-rays is unlikely, suggesting that different parts of the jet are responsible for those activities. However, we cannot rule out that an mm peak contemporaneous to the γ-ray one was missed due to the lack of observations at 230 GHz in 2010 May–June. The average γ-ray photon index of the source ($\Gamma_\gamma = 2.45 \pm 0.02$) is similar to the average value observed for FSRQ as well as for the FR II radio galaxies (in particular the SSRQ). Moreover, the average apparent isotropic luminosity of the source ($L_\gamma = 5.2 \times 10^{44}$ erg s^{-1}) is in agreement with the values observed for BL Lacs and radio galaxies. However, the lower luminosity with respect to SSRQ may be due to the close proximity of the source. Thus, taking into account its low redshift, the γ-ray properties of PKS 0521−36 are compatible with those observed in SSRQ and BLRG. In this context the strong flaring activity detected from this source by *Fermi*-LAT starting from 2010 June, with daily peak flux of 1–2 $\times$ 10^{-6} photons cm^{-2} s^{-1}, is very intriguing.

We discuss the γ-ray emission of this source in the framework of the 'spine-layer' scenario, with a fast spine surrounded by a slower layer, like in the case of the radio galaxy NGC 1275 (Tavecchio & Ghisellini 2014). We compare the SED of the flaring state (2010 June) with that of a low activity state (2010 February–March). We present three alternative models, corresponding to three different choices of the viewing angles $\theta_v = 6°$, $15°$, and $20°$. For the case with $\theta_v = 6°$ and $15°$ we obtain a good fit. According to the unification scheme for radio galaxies and blazars, reporting the SED obtained with $\theta_v = 15°$ as recorded by an observer at $\theta_v = 4°$, this SED would correspond to that of the 'aligned' counterpart of the radio galaxy. On the contrary, the resulting SED is strongly unbalanced towards the synchrotron luminosity (by a factor of ≈100), at odds with the typical blazar SED. This suggests that a viewing angle between 6° and 15° is preferred. In the spine-layer scenario proposed here the rapid variability observed during γ-ray flares favours a relatively small angle. However, we cannot rule out the possibility that PKS 0521−36 is an AGN seen at $\theta_v \sim 15°$ and its 'aligned' counterpart is a blazar belonging to a population of synchrotron-dominated objects.

This intermediate viewing angle is in agreement with the core dominance and the other radio properties observed, and thus with the classification of PKS 0521−36 as an SSRQ at low redshift or a BLRG. The strong γ-ray flaring activity observed by *Fermi*-LAT from this source indicates that SSRQ and BLRG may have relativistic jets as powerful as blazars. We noted that an increase of the γ-ray activity was observed for the SSRQ 3C 380 (Torresi & Grandi 2013), although at a flux level lower than that reached by PKS 0521−36.

The multifrequency observations and SED modelling presented here give important information about the characteristics of the AGN PKS 0521−36 and its classification. Further radio-to-γ-ray observations will be fundamental to investigate in even more detail the nature and the physical processes occurring in this source.

ACKNOWLEDGEMENTS

The *Fermi* LAT Collaboration acknowledges generous ongoing support from a number of agencies and institutes that have supported both the development and the operation of the LAT as well as scientific data analysis. These include the National Aeronautics and Space Administration and the Department of Energy in the United States, the Commissariat à l'Energie Atomique and the Centre National de la Recherche Scientifique/Institut National de Physique Nucléaire et de Physique des Particules in France, the Agenzia Spaziale Italiana and the Istituto Nazionale di Fisica Nucleare in Italy, the Ministry of Education, Culture, Sports, Science and Technology (MEXT), High Energy Accelerator Research Organization (KEK), and Japan Aerospace Exploration Agency (JAXA) in Japan, and the K. A. Wallenberg Foundation, the Swedish Research Council, and the Swedish National Space Board in Sweden. Additional support for science analysis during the operations phase is gratefully acknowledged from the Istituto Nazionale di Astrofisica in Italy and the Centre National d'Études Spatiales in France.

We thank the *Swift* team for making these observations possible, the duty scientists, and science planners. The Submillimeter Array is a joint project between the Smithsonian Astrophysical Observatory and the Academia Sinica Institute of Astronomy and Astrophysics and is funded by the Smithsonian Institution and the Academia Sinica. This research has made use of data from the University of Michigan Radio Astronomy Observatory which has been supported by the University of Michigan and by a series of grants from the National Science Foundation, most recently AST-0607523. This research was supported in part by NASA Fermi Guest Investigator awards NNX09AU16G, NNX10AP16G, NNX11AO13G, and NNX13AP18G. Part of this work is based on archival data, software, or online service provided by ASI Science Data Center (ASDC). The National Radio Astronomy Observatory is a facility of the National Science Foundation operated under cooperative agreement by Associated Universities, Inc. We thank S. Digel, D. J. Thompson, J. Perkins, D. Gasparrini, and the anonymous referee for useful comments and suggestions.

REFERENCES

Abdo A. A. et al., 2009a, ApJ, 707, 55
Abdo A. A. et al., 2009b, ApJS, 183, 46
Abdo A. A. et al., 2010a, ApJ, 714, L73
Abdo A. A. et al., 2010b, ApJ, 720, 912
Abdo A. A. et al., 2010c, ApJS, 188, 405
Acero F. et al., 2015, ApJS, preprint (arXiv:1501.02003)
Ackermann M. et al., 2012, ApJS, 203, 4
Ackermann M. et al., 2014, ApJ, 786, 157
Ackermann M. et al., 2015, ApJ, preprint (arXiv:1501.06054)
Aleksić J. et al., 2012, A&A, 539, L2
Aller M. F., Hughes P. A., Aller H. D., Latimer G. E., Hovatta T., 2014, ApJ, 791, 53
Atwood W. B. et al., 2009, ApJ, 697, 1071
Barthelmy S. D. et al., 2005, Space Sci. Rev., 120, 143
Baumgartner W. H., Tueller J., Markwardt C. B., Skinner G. K., Barthelmy S., Mushotzky R. F., Evans P. A., Gehrels N., 2013, ApJS, 207, 19
Birkinshaw M., Worrall D. M., Hardcastle M. J., 2002, MNRAS, 335, 142
Blandford R. D., Rees M. J., 1978, in Wolfe A. M., ed., BL Lac Objects. Univ. Pittsburgh Press, Pittsburgh, PA, p. 328
Bolton J. G., Clarke M. E., Ekers R. D., 1965, Aust. J. Phys., 18, 627
Bromberg O., Levinson A., 2009, ApJ, 699, 1274
Burbidge G., Hewitt A., 1987, AJ, 97, 1
Burrows D. N. et al., 2005, Space Sci. Rev., 120, 165
Cannon A., 2010, Astron. Telegram, 2591
Cardelli J. A., Clayton G. C., Mathis J. S., 1989, ApJ, 345, 245
Casandjian J.-M., Grenier I. A., 2008, A&A, 489, 849
Cheung C. C., Harris D. E., Stawarz Ł., 2007, ApJ, 663, L65
Ciprini S., 2013, Astron. Telegram, 4753
Condon J. J., Cotton W. D., Greisen E. W., Yin Q. F., Perley R. A., Taylor G. B., Broderick J. J., 1998, AJ, 115, 1693
D'Ammando F., Sokolovsky K. V., Iafrate G., Stark M., 2010, Astron. Telegram, 2689
D'Ammando F. et al., 2011, A&A, 529, A145
D'Ammando F. et al., 2012, MNRAS, 427, 893
D'Ammando F. et al., 2014, MNRAS, 438, 3521
Danziger I. J., Fosbury R. A. E., Goss W. M., Ekers R. D., 1979, MNRAS, 188, 415
Dermer C. D., Murase K., Takami H., 2012, ApJ, 755, 147
Ekers R. D. et al., 1989, MNRAS, 236, 737
Falomo R. et al., 2009, A&A, 501, 907
Fanaroff B. L., Riley J. M., 1974, MNRAS, 167, 31P
Foschini L. et al., 2006, A&A, 453, 829
Fuhrmann L. et al., 2014, MNRAS, 441, 1899
Gehrels N. et al., 2004, ApJ, 611, 1005
Ghisellini G., Tavecchio F., 2008, MNRAS, 386, L28
Ghisellini G., Tavecchio F., 2009, MNRAS, 397, 985
Ghisellini G., Tavecchio F., Chiaberge M., 2005, A&A, 432, 401
Ghisellini G., Tavecchio F., Foschini L., Ghirlanda G., 2011, MNRAS, 414, 2674
Giannios D., Uzdensky D. A., Begelman M. C., 2009, MNRAS, 395, L29
Giroletti M., Giovannini G., Taylor G. B., Falomo R., 2004, ApJ, 613, 752
Giroletti M. et al., 2012, A&A, 538, L10
Gurwell M. A., Peck A. B., Hostler S. R., Darrah M. R., Katz C. A., 2007, in Baker A. J., Glenn J., Harris A. I., Mangum J. G., Yun M. S., eds, ASP Conf. Ser. Vol. 375, From Z-Machines to ALMA: (Sub)Millimeter Spectroscopy of Galaxies. Astron. Soc. Pac., San Francisco, p. 234
Hartman R. C. et al., 1999, ApJS, 123, 79
Iafrate G., Longo F., D'Ammando F., 2010, Astron. Telegram, 2683
Kalberla P. M. W., Burton W. B., Hartmann D., Arnal E. M., Bajaja E., Morras R., Poppel W. G. L., 2005, A&A, 440, 775
Kataoka J. et al., 2010, ApJ, 715, 554
Kataoka J. et al., 2011, ApJ, 740, 29
Komatsu E. et al., 2009, ApJS, 180, 330
Lin Y. C., Bertsch D. L., Dingus B. L., 1995, ApJ, 442, 96
Marscher A., 2014, ApJ, 780, 87
Mattox J. R. et al., 1996, ApJ, 461, 396
Nolan P. L. et al., 2012, ApJS, 199, 31
Orr M. J. L., Browne I. W. A., 1982, MNRAS, 200, 1067
Pian E., Falomo R., Ghisellini G., Maraschi L., Sambruna R. M., Scarpa R., Treves A., 1996, ApJ, 459, 169
Raiteri C. M. et al., 2011, A&A, 534, A87
Raiteri C. M. et al., 2012, A&A, 545, A48
Roca-Sogorb M., Gómez J. L., Agudo I., Marscher A. P., Jorstad S. G., 2010, ApJ, 712, L160
Roming P. W. A. et al., 2005, Space Sci. Rev., 120, 95
Saito S., Stawarz Ł., Tanaka Y. T., Takahashi T., Madejski G., D'Ammando F., 2013, ApJ, 766, L11
Scarpa R., Falomo R., Pian E., 1995, A&A, 303, 730
Scarpa R., Urry C. M., Falomo R., Treves A., 1999, ApJ, 526, 643
Schlafly E. F., Finkbeiner D. P., 2011, ApJ, 737, 103
Slee O. B., 1977, Aust. J. Phys., Astrophys. Suppl., 43, 1
Sparks W. B., Biretta J. A., Macchetto F., 1994, ApJS, 90, 909
Stickel M., Padovani P., Urry C. M., Fried J. W., Kuehr H., 1991, ApJ, 374, 431
Stocke J. T., Morris S. L., Gioia I. M., Maccacaro T., Schild R., Wolter A., Fleming T. A., Henry J. P., 1991, ApJS, 76, 813
Tavecchio F., Ghisellini G., 2008, MNRAS, 385, L98
Tavecchio F., Ghisellini G., 2014, MNRAS, 443, 1224
Tavecchio F., Ghisellini G., Bonnoli G., Ghirlanda G., 2010, MNRAS, 405, L94
Tavecchio F., Becerra-Gonzalez J., Ghisellini G., Stamerra A., Bonnoli G., Foschini L., Maraschi L., 2011, A&A, 534, 86

Tavecchio F., Roncadelli M., Galanti G., Bonnoli G., 2012, Phys. Rev. D, 86, 085036
Thompson D. J. et al., 1995, ApJS, 101, 259
Tingay S. J., Edwards P. G., 2002, AJ, 124, 652
Torresi E., Grandi P., 2013, in Gómez J. L., ed., EPJ Web Conf. Vol. 61, The Innermost Regions of Relativistic Jets and Their Magnetic Fields. Published online, article no. 04006
Ulrich M. E., 1981, A&A, 103, L1
Urry C. M., Padovani P., 1995, PASP, 107, 803
Wilms J., Allen A., McCray R., 2000, ApJ, 542, 914
Wright A. E., Griffith M. R., Hunt A. J., Troup E., Burke B. F., Ekers R. D., 1996, ApJS, 103, 145

This paper has been typeset from a TEX/LATEX file prepared by the author.